Orographic signature on multiscale statistics of extreme rainfall: A storm-scale study

Mohammad Ebtehaj[1] and Efi Foufoula-Georgiou[1]

Received 23 February 2010; revised 14 September 2010; accepted 17 September 2010; published 4 December 2010.

[1] Rainfall intensity and spatiotemporal patterns often show a strong dependence on the underlying terrain. The main objective of this work is to study the statistical signature imprinted by orography on the spatial structure of rainfall and its temporal evolution at multiple scales, with the aim of developing a consistent theoretical basis for conditional downscaling of precipitation given the topographic information of the underlying terrain. The results of an extensive analysis of the high-resolution stage II Doppler radar data of the Rapidan storm, June 1995, over the Appalachian Mountains is reported in this study. The orographic signature on the elementary statistical structure of the precipitation fields is studied via a variable-intensity thresholding scheme. This signature is further explored at multiple scales via analysis of the dependence of precipitation fields on the underlying terrain both in Fourier and wavelet domains. The generalized normal distribution is found to be a suitable probability model to explain the variability of the rainfall wavelet coefficients and its dependence on the underlying elevations. These results provide a new perspective for more accurate statistical downscaling of orographic precipitation over complex terrain with emphasis on preservation of extremes.

Citation: Ebtehaj, M., and E. Foufoula-Georgiou (2010), Orographic signature on multiscale statistics of extreme rainfall: A storm-scale study, *J. Geophys. Res.*, *115*, D23112, doi:10.1029/2010JD014093.

1. Introduction

[2] There is evidence to suggest that the small-scale space-time structure of intense mountainous storms (sub-kilometer and subhour scales) has important hydrologic and geomorphic implications both in the short-term (e.g., triggering landslides and flash floods) and in the long-term evolution of landscapes [*Montgomery et al.*, 2001; *Roe*, 2005]. Also the consequences of extreme mountainous storms are often disastrous for the local and regional economy. For instance, the storm of 27 June 1995 over Madison County in Virginia caused a peak rainfall accumulation exceeding 600 mm in 6 h [*Smith et al.*, 1996] which produced flash flooding and triggered massive shallow landsliding and destructive debris flows across the region. Three fatalities and a total loss of property exceeding 200 million dollars [*Pontrelli et al.*, 1999] were reported. During the event of 28 July 1997, the city of Fort Collins in Colorado experienced a catastrophic flash flood that caused five fatalities and more than 200 million dollars in damage. Maximum accumulated rainfall for that storm exceeded 254 mm within 6 h [*Lin et al.*, 2001].

[3] In the long-term average, it is well known that the windward side of a mountainous range perpendicular to the moist wind flow receives more precipitation than the leeward side and leaves the dried air parcels to descend, resulting in a moisture-depleted region downslope called the rain shadow. This precipitation regime causes distinct climatic differences across the divide. This phenomenon is the first order and the most straightforward effect of the orographic signature on the spatial precipitation pattern. However, the full interaction of orography and rainfall spatiotemporal distribution is actually more complex and involves a variety of physical mechanisms. Forced lifting, differential advection of moist air aloft, convective currents initiated by mountain valley thermal gradients and cooling of warm moist air over snow covered mountains, individually or in combination, may enhance the intensity of rainfall production [e.g., *Barros and Kuligowski*, 1998]. *Roe* [2005] categorized the mechanisms of orographic precipitation as: (1) stable upslope ascent, (2) partial blocking of the impinging air mass, (3) down-valley flow induced by evaporative cooling, (4) leeside convergence, (5) convection owing to mechanical lifting above the level of free convection, and (6) seeder and feeder mechanism.

[4] Orographic terrains fuel the storm by intensifying the destabilizing forces and accelerating the updraft movement of moist-laden air masses. A significant number of the most heavy and disastrous precipitation events has been observed during the warm seasons over mesoscale mountainous ranges with several hundred kilometers in width such as the Rockies and the Appalachians in the United States and the Alps in Europe. Based on the analysis of several extreme storms in the United States (i.e., Black Hill flood, SD.,

[1]Department of Civil Engineering, Saint Anthony Falls Laboratory and National Center for Earth-Surface Dynamics, University of Minnesota–Twin Cities, Minneapolis, Minnesota, USA.

0148-0227/10/2010JD014093

1972; Big Thompson Canyon, CO., 1976; Fort Collins, CO., 1997; Madison County, VA., 1995), it can be concluded that the occurrence of such extreme events emerges from the coincidence of some common synoptic and mesoscale hydrometeorological mechanisms. Coexistence of a low-level and efficient moist airflow, steep gradient and strong quasi-stationary convective systems are common features in summer time orographically accelerated extreme storms [*Lin et al.*, 2001; *Bousquet and Smull*, 2003]. In such cases, most commonly, an area of intense pressure gradients is formed across the region under a quasi-stationary synoptic system which develops a low-level strongly moist upslope airflow. Orographic lifting provides the required energy to release the conditional instability and trigger a heavy rainfall. The quasi-stationary nature of the synoptic system develops a slow motion storm and magnifies more the hydromorphologic responses such as flash flooding and landsliding. Interestingly, studies of such storms in the United States show that a high value of the convective potential energy (CAPE) is not consistently observed in the storm environment [*Lin et al.*, 2001].

[5] In parallel to studying the driving physical mechanisms of precipitating systems, in recent decades considerable efforts have been expanded in understanding and quantifying the statistical structure of precipitation over different spatiotemporal scales [e.g., *Lovejoy and Mandelbrot*, 1985; *Lovejoy and Schertzer*, 1985; *Gupta and Waymire*, 1990, 1993; *Kumar and Foufoula-Georgiou*, 1993a, 1993b; *Perica and Foufoula-Georgiou*, 1996a, 1996b; *Veneziano et al.*, 1996; *Deidda*, 2000; *Deidda et al.*, 2004, 2006; *Badas et al.*, 2006]. Optimal parameterization and modeling of the multiscale behavior of rainfall fields often requires understanding of the conditional dependence of the statistical scaling parameters on some measures of the underlying physical processes. Along these lines, *Over and Gupta* [1994] investigated how the structure of rainfall at the mesoscale varies with time according to the large-scale dynamical forcing. *Perica and Foufoula-Georgiou* [1996a, 1996b] established predictive relationships between statistical characteristics of mesoscale rainfall and thermodynamics of the storm environment. *Harris et al.* [1996], *Purdy et al.* [2001], *Nykanen and Harris* [2003] and *Badas et al.* [2006] investigated the spatial structure of orographic rainfall in the context of multifractal analysis. To advance the previous findings and to gain insight toward a practical conditional parameterization of statistical downscaling schemes over complex terrains, the main goal of this work is to present the results of an extensive study on quantifying the scaling structure of an orographic precipitation system and relating it to the underlying topography in Fourier and wavelet domains. The rainfall data of an extreme storm over Madison County, Virginia (latitude 37.9859°N to 38.8763°N, longitude −77.8341°W to −78.9714°W) on 27 June 1995 are used in this study. The precipitation fields at 1 km × 1 km resolution (100 × 100 bins) are derived from the Sterling WSR-88D volume scan reflectivity data at every 6 min, using the Z-R conversion relationship $R = aZ^b$ with a = 0.0425 and b = 0.71 [see *Smith et al.*, 1996]. The underlying topographic elevations of the studied area at the same scale range between 66 and 1130 m above the mean sea level (see Figure 1a).

[6] In section 2, a concise description of the storm physical environment and the orographic precipitation mechanism is presented. In section 3, we establish a pyramidal variable-thresholding method for tracking the signature of orographic features especially on precipitation tail statistics. In section 4, the statistics and spatial scaling properties of the studied rainfall event are presented and discussed in real space, and in Fourier and wavelet domains. In section 5, it is shown that the shape of the distribution of wavelet coefficients and their spatial scaling law exhibit a systematic dependence on the underlying topography, providing thus the basis for more accurate parameterization. Some concluding remarks are made in section 6.

2. Storm Environment

[7] In this section, we briefly describe the mesoscale atmospheric conditions and the associated hydrologic and geomorphic responses of the Madison County storm of 27 June 1995. The reader is referred to *Pontrelli et al.* [1999] and *Smith et al.* [1996] for a comprehensive study of the storm environment and the measured hydrologic response, respectively. The activity of this storm can be divided into three main phases: "prestorm phase" from 0000 UTC to 0500 UTC, "storm phase" from 0500 to 2000 UTC and the "poststorm phase" which extends from 2000 to 2400 UTC. It needs to be mentioned that the "storm phase" consists of two major convective activities across the region: the first and larger one in spatial extent took place over the Piedmont plains and moved toward Madison County from 0500 to 1000 UTC; the second and larger one in intensity initiated near 1200 UTC, moved very slowly over the Madison county and produced flash flooding and massive debris flows.

[8] During the prestorm phase, a high-pressure system was positioned over New England pushing cold air southeastward into a warm low-pressure system centered off the coast of the Carolinas. Establishment of the synoptic high- and low-pressure systems over the region initiated a pronounced easterly cool and moist maritime airflow, impinging the eastern flank of the Appalachians. The lifted index value for the surface layer was slightly negative and the CAPE was relatively small (~150 J kg^{-1}) across the region. Atmospheric sounding at Sterling Radar Station (VA), indicated that the entire troposphere was near saturation [*Smith et al.*, 1996; *Pontrelli et al.*, 1999]. A high-pressure system built more southward, pressing the cold front into northern Virginia. Eventually, the easterly wind component and geographic features of the region in the Piedmont plains and Madison County triggered the first convective system around 0700 UTC. This front advanced southward and left the Madison County nearly rain-free and dissipated at 1100 UTC. This stage of the storm did not produce a major flash flooding but just increased the soil moisture content and left the region more vulnerable to excess precipitation. Around 1200 UTC, sounding information from the Sterling radar station signified that another strong convection was imminent. The level of free convection estimated at around 337m above the ground level, CAPE increased nearly to 600 J kg^{-1}, the lifted index lowered slightly to −2, and the precipitable water was about 50 mm [*Pontrelli et al.*, 1999]. Triggered by orography, the second strong convective system formed across the region during the late morning and early afternoon and prolonged to near 2000 UTC. This part of the storm was characterized by intense and slow moving rainy cells (~ 1.2 m s^{-1}) that produced a

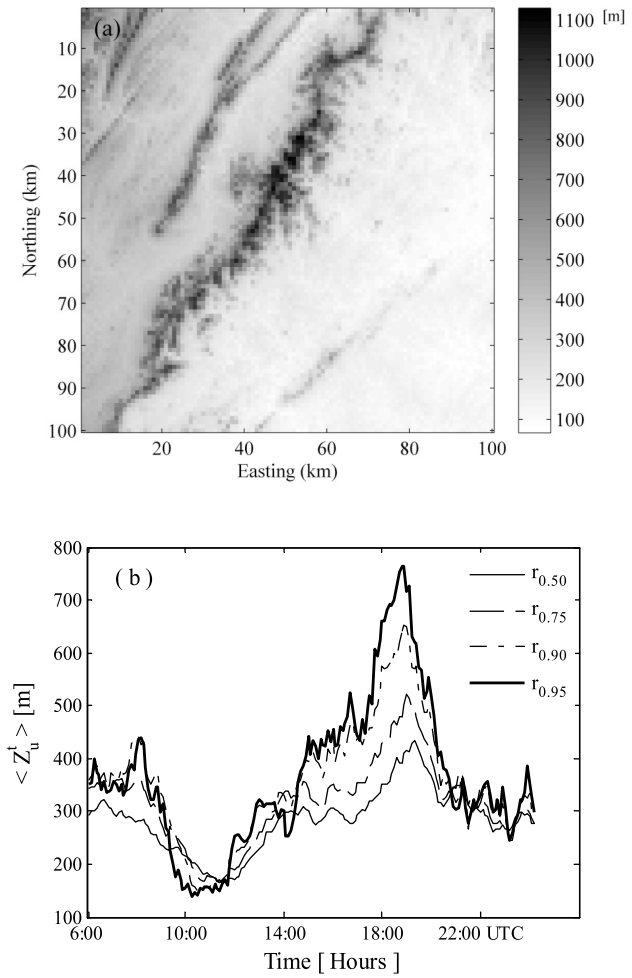

Figure 1. (a) Digital Elevation Model (DEM) of the studied area and (b) the spatial mean of the elevations underneath the rain cells $\langle Z_u^t \rangle$ defined at four different quantile levels u = 0.50, 0.75, 0.90, 0.95 (see text for definition).

peak discharge of 3000 m^3 s^{-1} at 1845 UTC in the Rapidan watershed near Ruckersville station [*Smith et al.*, 1996] and mobilized hundreds of shallow landslides into massive debris flows [*Wieczorek et al.*, 2004]. By 1800 UTC, the storm overtook the southern border of the Madison County and finally around 2000 UTC, the areal extent of the precipitation decreased and the system dissipated significantly. Some scattered convective activities were observed, but by 2400 UTC these activities disappeared completely. The most striking feature of this storm was its interaction with the underlying orography which along with other meteorological factors made the storm intense and very stationary [*Smith et al.*, 1996].

3. Statistical Signature of Orography on Rainfall Cells

[9] Several observations of spatial rainfall [e.g., *LeCam*, 1961; *Gupta and Waymire*, 1990] support the fact that the spatial organization of rainfall possesses a hierarchal structure: during the storm, small clusters of intense rainy cells are embedded inside the less intense and larger extent clusters of rain cells. In this section, we propose a simple methodology for extracting areas of intense rainfall activity and quantifying their underlying elevation for the purpose of characterizing dynamically the signature of topography on the statistics of rainfall intensity. At every snapshot of radar images, we define as "rain cells" all pixels of the rainfall fields over which the intensity exceeds a preassigned quantile of the overall storm rainfall intensity distribution. Delineating the geometry of the rain cells in time by this thresholding process, we dynamically analyzed the spatial statistics of the within-cells rainfall intensity with respect to the elevation of the topographic features underneath those cells.

[10] Let $F(.)$ denote the joint cumulative probability distribution of the nonzero rainfall intensities during the whole storm duration and $r_u = F^{-1}(u)$ be the quantile level associated with the probability of nonexceedance u (e.g., $u = 0.5$ to 0.95). At every radar image at time t, we denote by $R^t[k,l]$ the positive precipitation intensity in mm/h at location k, l and define as "rain cells," the set of values R_u^t over which the intensity exceeds the quantile value r_u,

$$R_u^t = \{R^t[k,l] | R^t[k,l] \geq r_u\}. \quad (1)$$

Likewise, let us denote the elevations underlying those rain cells as

$$Z_u^t = \{Z^t[k,l] | R^t[k,l] \geq r_u\}. \quad (2)$$

[11] To track the dynamics of the rainfall field's elementary statistics with respect to the underlying topography, the spatial average of the underlying elevations of the rain cells, $\langle Z_u^t \rangle$, is studied for different quantile levels. It can be observed (see Figure 1b) that during the first phase of the storm from 0600 to 1200 UTC, as the $\langle Z_u^t \rangle$ elevation curves decrease in time and collapse into each other for different quantile levels u, the rain cells tend to be distributed over a relatively flat area. However, during the second phase of the storm from 1200 to 2000 UTC, the magnitude of $\langle Z_u^t \rangle$ and its variability increases which means that the rain cells move upslope and get distributed over a region of steeper gradients.

[12] To quantify the signature of the underlying elevation on the statistics of rainfall intensity in time, we also tracked the evolution of the spatial average $\langle R_u^t \rangle$ and the spatial variance $Var(R_u^t)$ of the rain cell intensity for different quantile levels, over the whole storm duration. The results, reported in Figure 2, taken together with the results of Figure 1 show that there is a dependency among the tail statistics and underlying elevations of the rain cells. In other words, while the intense rain cells propagate over higher elevations during the storm evolution, the mean and the variance of the intensities of those cells grow in time (see Figures 2a and 2b), in a way that over high-elevation topography the variance grows even faster than the mean, especially for high quantiles (see Figure 2c, which depicts the coefficient of variation). Furthermore, analysis of the spatiotemporal average of rain cell intensities as a function of the underlying mean elevation for a range of quantiles

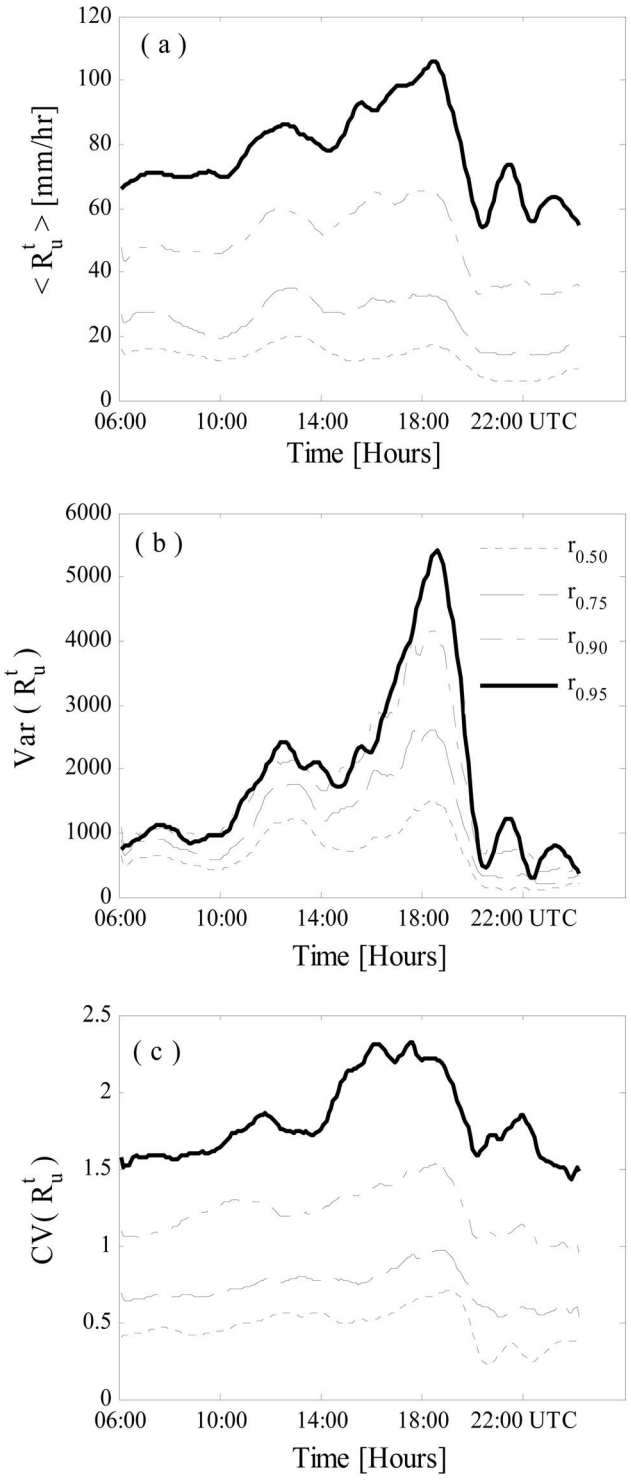

Figure 2. Time evolution of the (a) mean and (b) variance of rain cell intensities for different quantile levels. It is observed that while the storm moves toward higher topographic elevations (see Figure 1), both the mean and variance of the rain cells increase. It is also noted that the standard deviation cannot be linearly normalized by the mean as reflected in (c) the coefficient of variation, which does not remain invariant during the storm evolution.

defining the "rain cells" reveals an unexpected exponential relationship (see Figure 3) as

$$\overline{R}_u = z_0 \exp\left(k\overline{Z}_u\right), \tag{3}$$

where k and z_0 are constants, and $\overline{R}_u = \mathrm{E}[\langle R_u^t \rangle]$ and $\overline{Z}_u = \mathrm{E}[\langle Z_u^t \rangle]$ represent the ensemble (over all radar images during the storm evolution) spatial average of the rain cell intensities and the underlying elevations for the quantile level u, respectively. This exponential increase depicts the fact that the space-time dependence of extreme rain cluster intensity on topography, accelerates exponentially as one considers higher and higher-order quantiles. This relationship, which has to be investigated further for other storm systems, can provide a useful predictive relationship for parameterization of the orographic signature on rainfall elementary statistics.

4. Multiscale Analysis of Spatial Rainfall

[13] In section 3, rain cells were defined as rainy areas over which rain intensity exceeded a specified quantile threshold and it was found that the underlying topography gives rise to significant impacts on the first- and second-order statistics of the rainfall fields. By changing the quantile levels, cells of different size (scales) were investigated and it was shown that for the smaller scales (higher quantiles), the within-cell rainfall intensities and their variability became larger as rain cells moved toward higher elevations. In this section, using a formal multiresolution representation in real space, Fourier and wavelet domains, we pursue a different but complementary multiscaling analysis of the precipitation fields with respect to the underlying elevations.

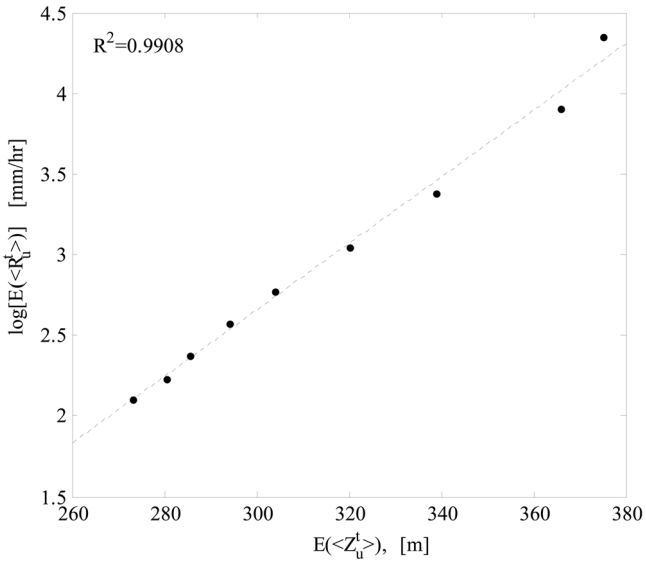

Figure 3. A semilog linear relationship indicates that the space-time average of the rain cell intensity increases exponentially with respect to their underlying elevations. Every circle represents a quantile level r_u, where u varies from 0.2 to 0.95 in increments of 0.1.

4.1. Scaling Manifestations in the Frequency and Real Space Domain

[14] The histogram of the spatial rainfall intensities is often very skewed with a broad dynamic range. To map the narrow range of many low-intensity values into a wider range of output levels, the logarithmic transformation is often an effective approach. To circumvent the problem of the zero intensity values in rainfall fields, a constant is typically added before the logs are taken, i.e., the transformation $\log(R^t[k,l] + c)$ is applied. However, since the location of zero intensity values is known anyway, the following invertible transformation is a preferred alternative,

$$\psi^t[k,l] = \begin{cases} 0 & \text{if } R^t[k,l] = 0 \\ \log(R^t[k,l]) & \text{otherwise} \end{cases}, \tag{4}$$

where the log(.) denotes natural logarithm. In particular, this transformation allows the entire real axis to be available for statistical computation, it makes the histogram of the field more Gaussian-like (e.g., see Figure 4f) and as such it facilitates the detection and estimation of scale invariance [*Ruderman*, 1994; *Huang and Mumford*, 1999]. It is worth noting that, as the log function is a monotonic transformation, the overall scaling law of the process would not be distorted in Fourier and real space under this transformation. In the sequel, unless otherwise noted, all analyses are performed on the log-transformed rainfall fields according to equation (4).

[15] Knowing that the inner product and norms in L^2(R) are conserved by the Fourier transform (i.e., Parseval theorem), the Fourier expansion has been widely used for detecting the second-order scaling laws of geophysical processes. Using the 2D Discrete Fourier Transformation, the power spectra (i.e., square of the absolute values of the Fourier coefficients) of the $\psi^t[k,l]$ have been computed for each of the radar images over the whole storm duration of 18 h (180 radar snapshots at every 6 min). The output of the transformation is rearranged by moving the zero-frequency components to the center of the spectrum for visualization purposes. To reduce the measurement noise effect and have a robust estimation in the spectral domain, an ensemble representation is obtained by averaging the spectra of rainfall images over the entire period of the storm. A contour plot of the ensemble power spectral density in the frequency domain is shown in Figure 5. It is observed that the storm spectral signature exhibits an anisotropic pattern and interestingly, this shape shows an elliptic regularity with its major axis perpendicular to the Appalachian ridge line (see the dashed line in Figure 5) for low frequencies and aligned to the mountain ridge line at higher-frequency components. This directional behavior speaks for the organization and elongation of intense rain cells (small-scale features) perpendicular to the mountain ridge, an isotropic energy distribution at intermediate scales and a coherency along the prevailing topography at much larger scales.

[16] The 2D spectral density is mapped into a one-dimensional representation via averaging over all angles about the center of the spectrum. As shown in Figure 6, for the radial frequency interval [0.03, 0.50] cycles/pixel corresponding to scales of 2 to 32 km in real space, a clear log-log linearity of the ensemble spectrum of the rainfall field is observed. This confirms that the spatial distribution of the energy (i.e., variance) over radial frequencies $f_r = \sqrt{f_k^2 + f_l^2}$ admits a power law scaling relationship in the following form:

$$S_R(f_r) \propto 1/f_r^{\beta_e}, \tag{5}$$

where the slope of the ensemble spectrum is $\beta_e \sim 2.5$.

[17] It is interesting to ask how the spectral slope varies as the storm evolves over the mountain range. For the same frequency interval, the estimated exponents of the directionally averaged spectrum for each of the radar images are plotted versus time and $\langle Z^t_{0.95} \rangle$ in Figures 7a and 7b, respectively. It is seen that the spectral slope ranges from 2.1 to 2.7 with a dependency on the underlying topography during the storm period from 0600 to 2000 UTC. In short, while the storm was developing over the low-elevation terrain ($\langle Z^t_{0.95} \rangle < 300m$), the spectral slope is larger indicating a stronger spatial self-coherence (i.e., the energy content drops off faster from larger-scale features down to cells of very small size). When the storm evolves over the mountain barrier ($\langle Z^t_{0.95} \rangle > 400m$) the energy is distributed more uniformly across different ranges of scales, which implies that the spatial autocorrelation structure of the fields weakens when the orographic effect is more significant. In between (elevations of 300 to 400 m) the storm is in a transitional state with a widely varying spectral slope (see Figure 1b).

[18] This scaling behavior in the Fourier domain can be translated into real space which is more conducive to understanding the correlation structure associated with the observed power law spectral signature. Defining the 2D autocorrelation function of an image as the expected value of the component-wise product of the image with itself at different spatial translations $[d_k,d_l]$,

$$C[d_k, d_l] = \langle \psi[k,l], \psi[k + d_k, l + d_l] \rangle, \tag{6}$$

Ruderman [1997] analytically proved that for a field with power law spectrum of slope $\beta > 2$, the directional average of its autocorrelation function has the following form:

$$C(d_r) = c_1 - c_2 d_r^{\beta - 2}, \tag{7}$$

where c_1 and c_2 are positive constants and $d_r = \sqrt{d_k^2 + d_l^2}$. By expanding equation (6), it can be shown that for a field with this correlation structure, the variogram

$$\gamma(d_r) = \langle |\psi[k,l] - \psi[k + d_k, l + d_l]|^2 \rangle \tag{8}$$

also exhibits a similar power law relationship.

[19] The variograms of the rainfall fields are shown in Figure 8 in a log-log plot and the estimated slope in the scaling range of $2 \le d_r \le 32$ *km* confirms the spectral analysis in an average sense and shows that the variogram follows a power law scaling with an estimated slope of ~0.4–0.5. By inspection, the sum of the autocorrelation function in equation (7) with $\beta > 2$ includes a divergent p series which in other words signifies a nonsummable autocorrelation function [e.g., see *Beran*, 1994] over radial translations and speaks for the evidence of long-range dependence in spatial rainfall intensities.

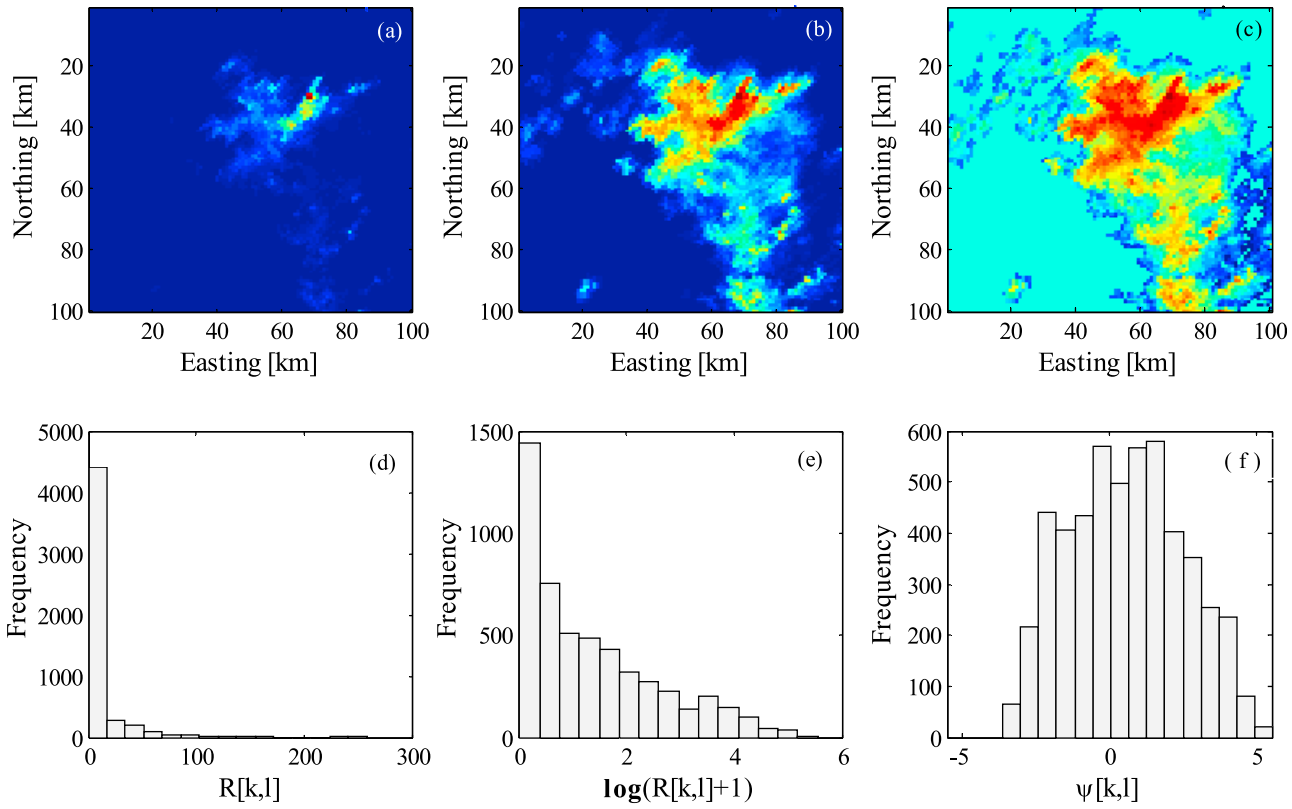

Figure 4. (a) Image of the Rapidan storm radar snapshot $R[k,l]$ at 0800 UTC. (b) Image of the $\log(R[k,l] + 1)$. (c) Image of the transformed rainfall fields $\psi[k,l]$ according to equation (4). (d, e, and f) The corresponding histograms of the nonzero intensity values of Figures 4a, 4b, and 4c, respectively. Throughout this study, the transformation of equation (4) displayed in Figures 4c and 4f has been employed.

[20] Up to this point, the second-order scale invariance properties of the rainfall field in the Fourier domain and real space have been studied and some connections of this scaling behavior with respect to the underlying elevations have been explored. In the domain of Gaussian self-similar random fields this characterization can fully explain the scaling properties of the process. However, if the process is not Gaussian, higher-order statistical moments over different scales (resolutions) need to be computed to test the presence of scaling. This can be accomplished by "coarse graining" the field at the original (highest) resolution to obtain fields at successively lower resolutions. Defining the original spatial rainfall as an image of size $N \times N$, a coarse-grained field at scale λ can be obtained by passing a non-overlapping averaging filter of size $\lambda \times \lambda$ over the field,

$$\psi_\lambda\left[k',l'\right] = 1/\lambda^2 \sum_{k,l}^{\lambda} \psi[k,l], \tag{9}$$

where the $\psi_\lambda[k',l']$ is a field of the same areal coverage as $\psi[k,l]$ but decimated by a factor λ in each dimension. As formation of local intense convective cells imposes a sharp spatial variation on precipitation intensity values, the magnitude of the gradient of a precipitation field implicitly represents the intensity of the rainfall convective activities. It is known that for a strictly self-similar Gaussian field the distributions of the local gradient $\nabla\psi_\lambda[k',l']$ standardized by their corresponding means are independent of λ and collapse into an identical shape of the Rayleigh density function [*Ruderman*, 1994].

[21] For this purpose, we focused on the distributions of the magnitude of the local gradients of the coarse grained fields at different scales λ.

$$\left|\nabla\psi_\lambda\left[k',l'\right]\right| = \sqrt{\left(\frac{\partial\psi_\lambda[k',l']}{\partial k'}\right)^2 + \left(\frac{\partial\psi_\lambda[k',l']}{\partial l'}\right)^2}. \tag{10}$$

[22] Distributions of the local gradients of the rainfall images are presented in log probability for $\lambda \in \{1,2\ km\}$ in Figure 9. It is seen that the histograms do not collapse on each other, particularly over the tail, which implies that simple scaling may not hold true. The tail is also thicker than the Rayleigh distribution and in general the peaks of the histograms locate before the maximum of the Rayleigh density. The same trend is revealed for larger scales; however, naturally the histograms tend gradually to the shape of the Rayleigh distribution as the scale increases. Interestingly, it is also observed that even by averaging the field over larger scales (16×16 km) the gradient fields cannot be fully explained in the Gaussian domain. This mainly arises because of the strong spatial correlation of the field,

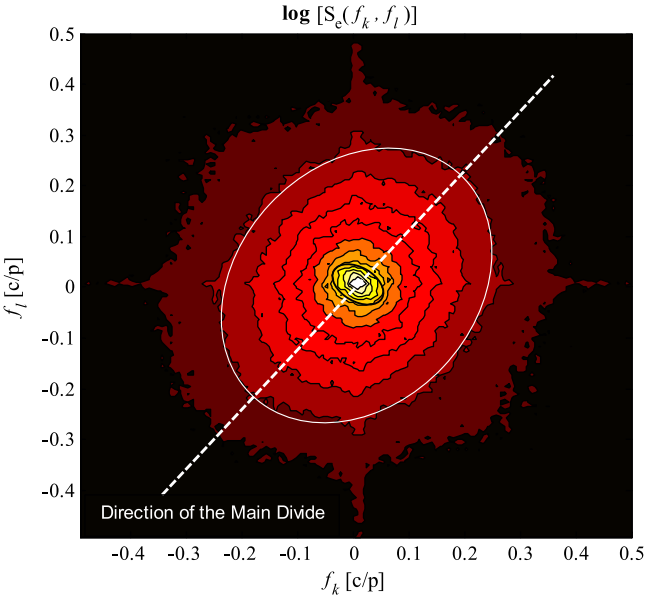

Figure 5. Two-dimensional ensemble average spectral signature of the Rapidan storm. The power spectrum is centered at frequencies $f_k = f_l = 0$ and divided by 12 equally spaced contour lines. The dashed line displays the approximate direction of the underlying main divide.

knowing that the central limit theorem holds true only for independent or weakly dependent random variables.

4.2. Filter Response and Parameterization of Rainfall Fluctuations

[23] In section 4.1, it was revealed that not only the studied rainfall fields deviate from the Gaussian domain of attraction but also they cannot be fully explained by simple scaling. In this section, scaling of the rainfall fields is explored in the wavelet domain with particular emphasis on precipitation extreme values (i.e., thick tails) to establish a framework for conditional downscaling of rainfall with respect to the underlying elevations.

[24] In recent years, wavelet decomposition has played an important role in the area of multiscale analysis of $1/f$ processes [*Wornell and Oppenheim*, 1992; *Flandrin*, 1992; *Kaplan and Kuo*,1993; *Abry and Sellan*, 1996; *Zhang et al.*, 2004] and also has been successfully applied for efficient multiscale encoding of rainfall fields [e.g., *Kumar and Foufoula-Georgiou*, 1993a, 1993b]. Using 2D wavelet decomposition, a spatial signal with finite energy content is encoded into a set of approximation coefficients $a_j[k,l]$ and a set of zero mean detail coefficients $d_j[k,l]$ with respect to the shifted and dilated version of a complete set of orthonormal basis functions. Instead of the inner product formalism for the computation of the wavelet coefficients, starting from any given resolution of an image, these wavelet coefficients can be computed recursively by convolution of the signal with a cascade of discrete filter banks [*Mallat*, 1989] from fine to coarse scales in which at each recursion the size of the image is decimated by a factor of two. This decomposition procedure also allows an additive perfect reconstruction of the image, knowing the root-scale coarse approximation coefficients $a_0[k,l]$ and sequences of detail coefficients $d_j[k,l]$ at finer scales.

[25] Here to study the scaling properties of the rainfall fields, we employ a basic form of the wavelet transformation using the two-dimensional Haar band-pass filters (Figure 10). This filter bank is passed recursively over a 2D field in a nonoverlapping scheme to compute the high and low band-pass coefficients from fine-to-coarse scales. Starting with an image of size $2^{j+1} \times 2^{j+1}$, applying the high and low band-pass filters simultaneously, we can compute the first-level directional details and approximation wavelet coefficients, which are images of size $2^j \times 2^j$. By repeating this procedure recursively in $j+1$ levels, this process can go on until we get an image of size 1×1 for the approximation coefficients. Hence, provided that the image at a coarse scale is given, knowing exactly the sequence of wavelet detail coefficients, a perfect reconstruction from coarse-to-fine scale is possible via

$$a_{j+1}[2k,2l] = a_j[k,l]/2 + \left(d_j^h[k,l] + d_j^v[k,l] + d_j^d[k,l]\right)/2, \quad (11)$$

where the superscripts *h, v* and *d*, denote the horizontal, vertical and diagonal wavelet coefficients. Here, $a_{j+1}[2k,2l]$ just means that the number of image pixels doubles at every reconstruction recursion [see also *Perica and Foufoula-Georgiou*, 1996a; *Riedi et al.*, 1999].

[26] Recalling the theory of multiplicative random cascades [e.g., *Gupta and Waymire*, 1993], the spatial rainfall fields in a finite range of scales can be reconstructed using the following dyadic recursion formalism from coarse-to-fine scales:

$$R_{j+1} = R_j \zeta_j, \quad \langle \zeta_j \rangle = 1, \quad (12)$$

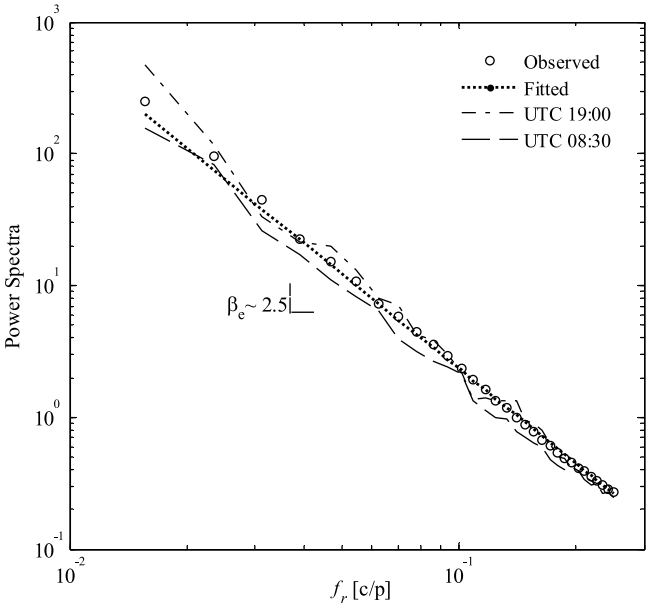

Figure 6. Open circles show the one-dimensional representation of the rainfall field ensemble average Fourier power spectrum, and the dotted line represents a fitted least square linear model ($R^2 = 0.96$). The angular averaged power spectra of the rainfall fields at two different instants of time are also depicted (dashed lines). The log-log linearity of the power spectrum confirms the presence of second-order scaling in the range of 2–32 km.

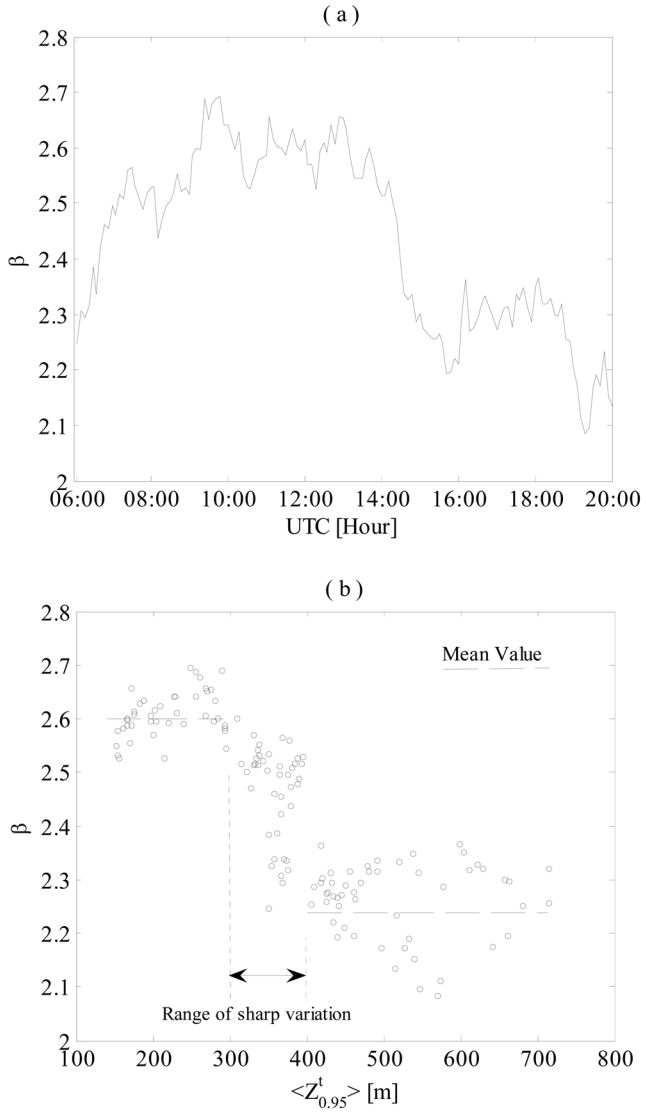

Figure 7. (a) Spectral slope of each of the radar images versus time during the storm period and (b) spectral slope versus the rain cell elevation $\langle Z^t_{0.95} \rangle$. Spectral slope decreases as the average underlying elevation of the rain cells increases. This dependence implies that the surface of the rainfall images becomes rougher in a geometrical sense with weaker correlation structure while it is intensified by orographic interaction.

where R_j denotes the rainfall process at resolution 2^j and ζ_j is a random multiplier or cascade generator with the expectation value of unity. By taking the logarithm of both sides, this stochastic structure can be described in an additive Multiresolution Markovian form with a zero mean random component,

$$\psi_{j+1} = \psi_j + \varepsilon_j, \ \varepsilon_j \sim^d \ln(\zeta_j), \quad \langle \varepsilon \rangle = 0. \tag{13}$$

[27] Comparing equations (12) and (13), it can be concluded that the 2D discrete Haar Wavelet transform of the log-transformed rainfall images provides an efficient means for characterizing the statistics of the cascade generator in a logarithmic space. Indeed, provided that the wavelet decomposition works as a whitening filter and knowing a parametric probability model for the wavelet detail coefficients, this formalism allows one to reconstruct or downscale the rainfall field from coarse-to-fine scales on a quad tree cascade of wavelet coefficients (see Figure 11).

[28] In this work, we did not focus on reconstruction or downscaling of the rainfall field on the basis of the described procedure and left it for future study. However, we concentrated our attention on the characterization of the marginal distribution of the detail wavelet coefficients of the log-intensity rainfall fields and their dependence on the underlying topography. In Figure 12, the studentized distributions (i.e., unit variance) of the sum of the nonzero wavelet subbands at all orientations are demonstrated in log probability for all Rapidan storm radar snapshots at one level of decomposition. As shown, the average behavior of the distribution in the log probability space appears to be leptokurtic with a more acute peak around the mean and thicker tail than the parabolic tail of a Gaussian distribution (Figure 12, dashed line). Assuming that the wavelet coefficients are defined in $L^2(\mathrm{R})$, this tail behavior may be intuitively explained by a symmetric distribution with double exponential tails (i.e., $\exp\{|x|^\alpha\}$) with an exponent α less than 2 which describes the tail of a Gaussian random variable. The family of generalized Gaussian (GG) distributions (see Figure 13), also known as the Generalized Laplace and/or Exponential Power Distribution in the statistical literature, is a class of probability density functions that can potentially model this sort of heavy tail behavior [e.g., *Huang and Mumford*, 1999]. There are different parameterizations for this class of distribution functions in the literature; however, the early form was first introduced by *Subbotin* [1923] and well established by *Vianelli* [1963, 1983]. In this work, we used a symmetric zero mean form of this class, according to the proposed parameterization by *Nadarajah* [2005] as follows:

$$f_X(x) = \frac{\alpha}{2s\Gamma(1/\alpha)} \exp\left\{ -\left|\frac{x}{s}\right|^\alpha \right\} \sim GG(s, \alpha), \tag{14}$$

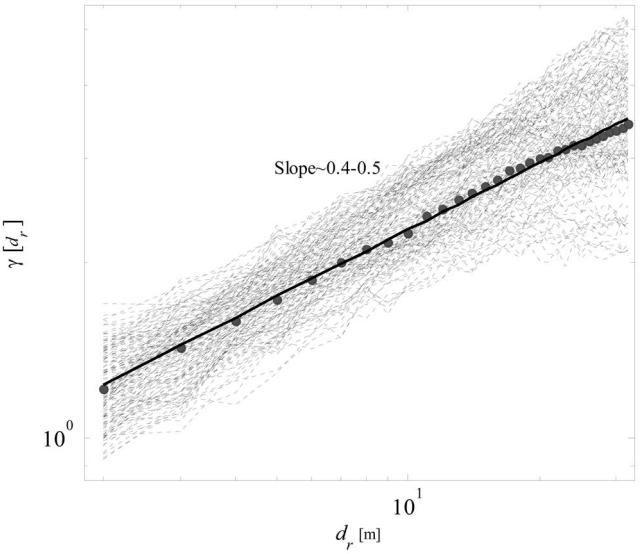

Figure 8. Variogram of all storm radar snapshots in a log-log plot. The observed slopes confirm the power law behavior of the spectra (see Figure 6) and long-range dependence.

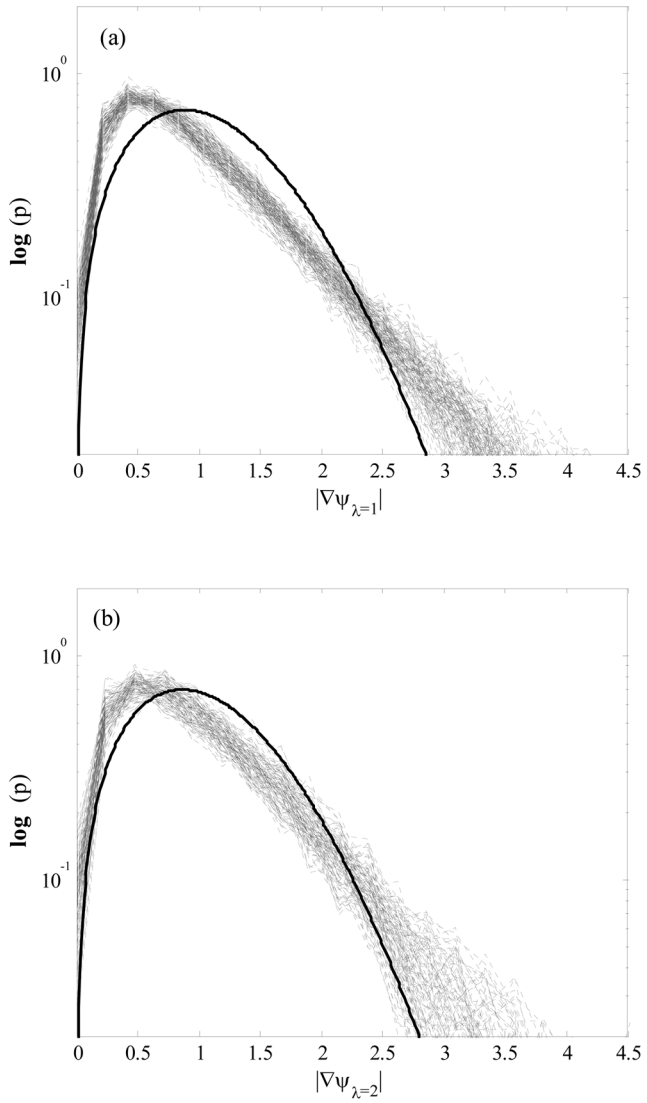

Figure 9. Dashed lines represent the distribution of the gradient of the normalized log-intensity rainfall fields $\psi^t[k,l]$ for $\lambda \in \{1\ 2\}$ km over the entire period of the storm. Solid line is a Rayleigh distribution fitted to the average histogram. The tail behavior indicates a deviation from Gaussianity.

where $x \in \mathrm{R}$, and the s and α are positive real-valued width and tail parameters of the distribution.

[29] Laplace and normal densities are particular cases of the GG density when $\alpha = 1$ and *2*, respectively. In the limiting case when $\alpha \to +\infty$, the density would approach a uniform distribution on $(-s, +s)$ and it would be a Dirac delta function when $\alpha \to 0$. The tail probability of this distribution is summable and by the usual central limit theorem, the sum of random samples from this distribution tends to the standard normal distribution. In other words, the density does not preserve its shape under aggregation except for $\alpha = 2$ [*Nadarajah*, 2005]. All of the central moments of the distribution are finite and the density can be fully characterized knowing the second- and fourth-order moments,

$$\mathrm{E}[X^2] = s^2\Gamma(3/\alpha)/\Gamma(1/\alpha), \mathrm{E}[X^4] = s^2\Gamma(5/\alpha)/\Gamma(1/\alpha). \quad (15)$$

[30] Studying the storm radar scans, it is found that the GG distribution could be an admissible model for explaining the variability of the wavelet detail coefficients. The studentized histogram and the fitted model for the radar image at the 0830 UTC are demonstrated in Figure 14 at three different scales. Fitting can be performed based on the conventional Method of Moment (MM) or the Maximum Likelihood (ML) estimation procedures. *Rahman and Gokhale* [1996] found that both methods perform similarly for $\alpha < 2$. Using the MM for this case and the Kolmogorov–Smirnov (K-S) goodness of fit test, it is revealed that we can explain those coefficients by the GG distribution with high degree of statistical confidence, i.e., at the 95% significance level.

[31] Scaling of the wavelet detail coefficients in a multifractal context manifests itself as a power law behavior of their qth-order moments [e.g., see *Mandelbrot et al.*, 1997; *Abry et al.*, 2004],

$$\mathrm{E}\{|d_j[k,l]|^q\} = c_q 2^{-j\tau_q}, \quad (16)$$

for a given finite range of scales $j_{\mathrm{Min}} \le j \le j_{\mathrm{Max}}$, where $j_{\mathrm{Max}} / j_{\mathrm{Min}} \gg 1$ and for all q such that $\mathrm{E}\{|d_j[k,l]|^q\}$ is finite over an interval$[0, q_{\mathrm{max}}]$. The τ_q is usually referred to as the scaling exponent and c_q is a prefactor. When the scaling exponent can be explained linearly as $\tau_q = qH$, the wavelet coefficients are monofractal or simple scaling and the exponent H denotes the self-similarity index.

[32] To describe the spatial scaling law of wavelet coefficients in a robust statistical sense, all of the available radar images of the storm are studied in the wavelet space, using the described Haar filter banks. Focusing on a parsimonious representation, the second- and fourth-order moments of the wavelet coefficients of all log-transformed rainfall fields for four levels of decomposition are computed and illustrated in Figure 15. The semilog linearity of the moments versus decomposition levels signifies that not only the variance but also the fourth-order moments of the wavelet coefficients are power law scaling in an average sense.

[33] From equation (15), the tail parameter of the GG distribution can be numerically estimated knowing the sample kurtosis κ,

$$\kappa = [\Gamma(5/\alpha)\Gamma(1/\alpha)]/[\Gamma(3/\alpha)]^2. \quad (17)$$

[34] Therefore, the scaling law of the tail parameter in dyadic scales can be derived analytically by characterizing the kurtosis at different resolutions as follows:

$$\kappa(j) = \frac{c_4}{(c_2)^2} 2^{-j[\tau_4 - 2\tau_2]}. \quad (18)$$

By definition, for simple scaling processes (i.e., $\tau_q = qH$) the thickness of the tail at different scales remains invariant. Analyzing the expected values of second- and fourth-order moments for the entire data set (see Figure 15), it is revealed that in an average sense $\mathrm{E}[\tau_4/\tau_2] \cong 2$ and the wavelet coefficients behave similar to a simple scaling (monofractal) signal. However, their kurtosis is greater than the Gaussian case $\kappa \cong 4.8 > 3$ which is equivalent to the tail parameter $\alpha \cong 1.2$ in a generalized Gaussian density.

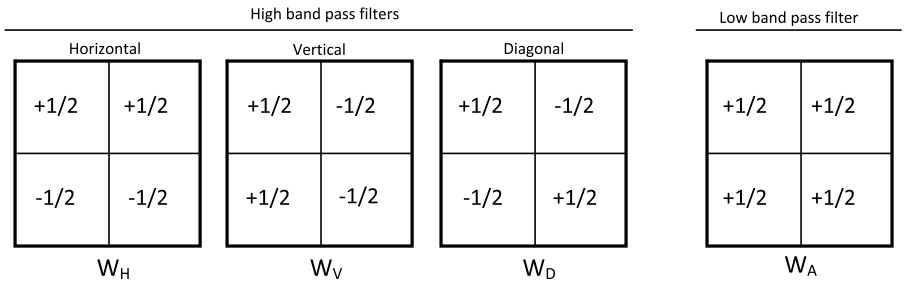

Figure 10. High and low band-pass Haar wavelet filters are applied in nonoverlapping 2 × 2 blocks on the rainfall images recursively to obtain wavelet subband coefficients at different resolutions.

[35] Linearity of the second-order moment in Figure 15 confirms the presence of 1/*f* spectra and knowing the process fractality, using equation (15) a similar power law scaling can be derived for the width parameter *s* of the GG distribution; see Figure 16. It needs to be mentioned that this monofractal property of the wavelet coefficients does not necessarily mean that any reconstructed process from coarse-to-fine scales, on the basis of the described approach, is also monofractal. The GG distribution does not preserve its shape under aggregation except for $\alpha = 2$ and the sum of the GG random variables tends to a Gaussian density in the limiting case. Therefore, as the wavelet cascade evolves from coarse-to-fine scales by adding GG random numbers in log scale, the distribution of the cascade tends to the normal density which means that the distribution of the original field tends to a log-normal density.

5. Conditional Multiscaling Analysis

[36] In section 4, transforming the rainfall radar images into a log space, the stochastic nature of the rainfall wavelet fluctuations (i.e., detail coefficients) and their scaling properties were studied using the GG density. According to the described formalism, while one wants to downscale stochastically a remotely sensed rainfall image from coarse-to-fine (say $\lambda_c \rightarrow \lambda_f$) scales at the time step *t*, the parameters of the probability density of the wavelet coefficients (i.e., GG density) need to be estimated at the available root-scale λ_c. Consequently, some important questions may arise on how these parameters are to be estimated based on the precipitation data available at the coarse scale, say $\lambda_c = 8$ km. Is there any functional relationship between those parameters and the underlying topography while the storm evolves in time? Can one use the information content of the underlying topography to reduce the estimation error of those downscaling parameters? Motivated by the need to establish an efficient downscaling scheme over complex terrain, this section is devoted to analyzing the dynamical evolution of the GG density parameters (α, *s*) with respect to the orographic signature on the rainfall field at a given coarse scale.

[37] To capture the signature of landscape features on rainfall variability at different scales, a statistical measure which accounts for the joint information content of the rainfall field and the underlying elevations is defined. Specifically, we define a time- and scale-dependent orographic index as the cross correlation of the precipitation fields R^t_λ with the underlying elevations Z^t_λ at a particular scale λ,

$$OI^t_\lambda = \langle R^t_\lambda, Z^t_\lambda \rangle / \sqrt{\langle R^t_\lambda, R^t_\lambda \rangle \langle Z^t_\lambda, Z^t_\lambda \rangle}, \tag{19}$$

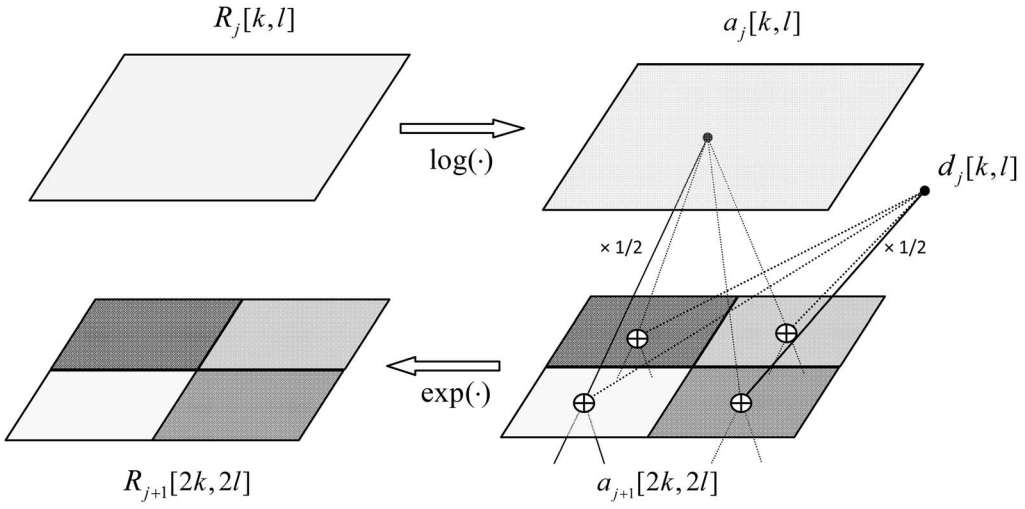

Figure 11. Quad-tree structure of Haar wavelet coefficients for reconstruction of a spatial rainfall field. Assuming $a_j[k,l] = \psi_j$ in equation (13) and a parametric probability model for $d_j[k,l]$, we can synthetically reconstruct the approximation coefficients and the rainfall field at the next higher resolution level $j+1$.

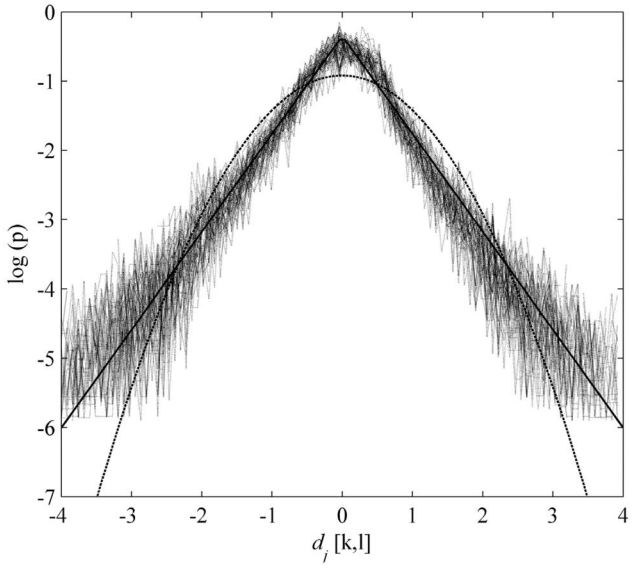

Figure 12. Distribution of the wavelet detail coefficients for all log-intensity radar images of the Rapidan storm. The distributions are plotted in log probability for clear illustration of the non-Gaussian nature of the tail. The solid line shows the average histogram behavior, and the dotted line denotes the standard normal distribution.

where $\langle X, Y \rangle$ denotes the expected value of the component-wise product of X and Y. Accordingly, the Orographic Index OI^t_λ is a normalized index between 0 and 1 which potentially reflects the significance of the orographic signature on the rainfall field in the sense that when the orographic index is found to grow in time, on average, the more intense rain

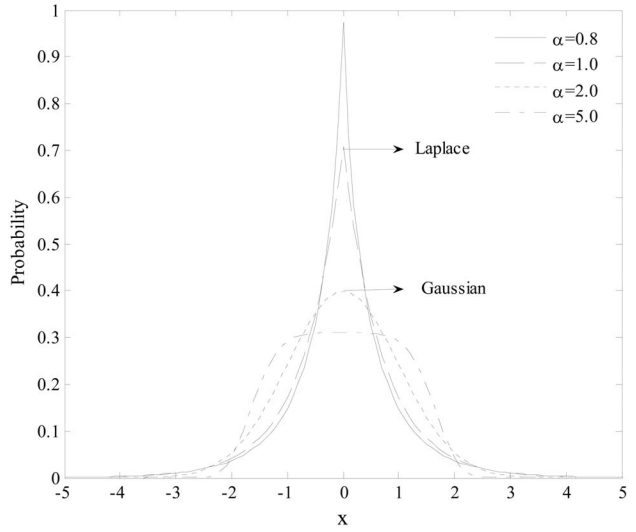

Figure 13. The generalized Gaussian is a flexible family of distributions which in a particular parameterization allows a symmetric probability continuum spanning from a Dirac delta function ($\alpha \to 0$) to a uniform density ($\alpha \to \infty$). In the range of $0 < \alpha < 2$, the density has a thicker tail than a standard normal distribution and the tail becomes thinner for $\alpha > 2$.

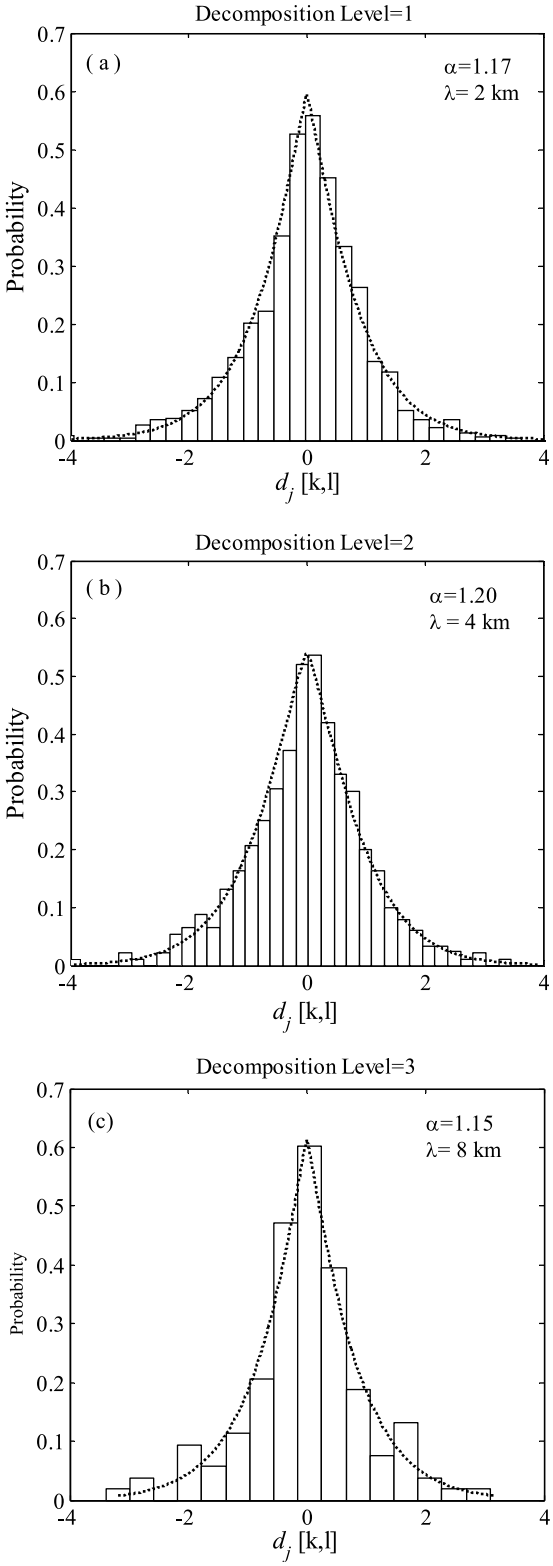

Figure 14. Fitted generalized Gaussian distribution to the studentized wavelet coefficients of the horizontal subband in three decomposition levels (i.e., $\lambda \in \{2, 4, 8\}$ km) at 0830 UTC. In this case, the *K-S* test results indicate that at the 95% confidence level the observed wavelet coefficients are samples from the selected family of distributions.

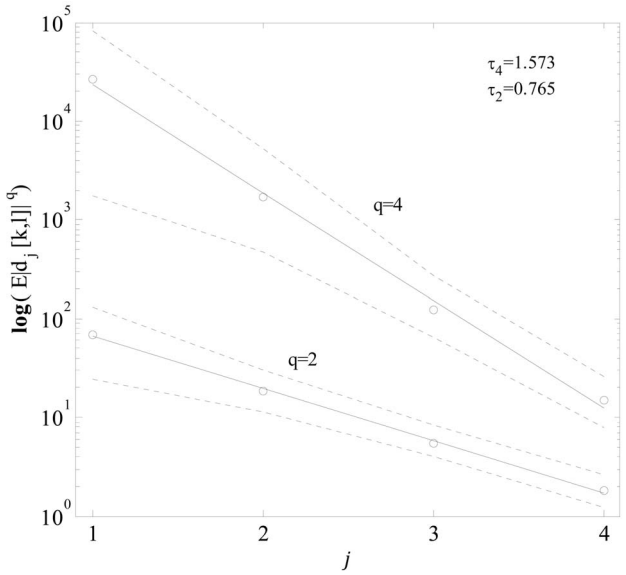

Figure 15. Second- and fourth-order moments of the wavelet coefficients at different resolutions (i.e., $\lambda \in \{16, 8, 4, 2\}$ km) for all storm radar images. Open circles show the mean values (ensemble average over all radar images), and the dashed lines represent the corresponding 95% confidence intervals of the estimates. The results of the least square fitting (solid lines) indicate that the expected values of these moments exhibit power law scaling with a high degree of confidence ($R^2 > 0.96$).

cells are formed over higher elevations. For the storm period (i.e., 0600–2000 UTC) at every radar snapshot, Figures 17a and 17b display the scatterplots of the parameters of the fitted GG distributions versus the orographic index computed at the scale λ_c = 8 km. Evidently, as the orographic index increases, both the width s and the tail parameter α of the rainfall fluctuations increase. In other words, while high-intensity precipitation cells are developed over areas of higher elevation, the energy of the rainfall wavelet fluctuations in terms of their standard deviation increases and they become more organized with thinner tails.

[38] Although the dependence of the parameters on the orographic index is evident in our case study, linear predictive relationships explain less than 50% of the variability as the correlation coefficients are between 0.5 and 0.7 ($R^2 < 0.5$). Therefore, in the sequel efforts are focused on quantifying how much the mean square error of the parameter estimation may be improved by discrete conditioning on the orographic index, without relying on the assumption of linear dependence. To this end, nonparametric conditioning is performed on nonoverlapping subsets of the storm orographic indices at λ_c = 8 km. To encode the maximum amount of extractable information content in a least square sense, the set of computed orographic indices in time is partitioned into k mutually exclusive and collectively exhaustive subsets to estimate the conditional expected value of the downscaling parameters at each partitioning by

$$\mathrm{E}[\theta|OI_k] = \sum_{a \in OI_k} a\mathrm{P}(\theta = a|OI_k), \qquad (20)$$

where $\theta \in \{\alpha, s\}$, "a" denotes any value of the parameter "α" or "s" estimated on any member of the subset k and $\mathrm{P}(\theta = a|OI_k)$ is a uniform conditional probability measure with $\mathrm{P}(OI_k) > 0$.

[39] The degree of improvement in the variance of the estimation error of those parameters θ given the orographic index can be calculated on the basis of the following general relationship [*Fristedt et al.*, 2007]:

$$\mathrm{E}[\theta - \mathrm{E}(\theta)]^2 - \mathrm{E}[\theta - \mathrm{E}(\theta|OI_k)]^2 = \mathrm{E}[\mathrm{E}(\theta|OI_k) - \mathrm{E}(\theta)]^2. \qquad (21)$$

For instance, according to a partitioning scheme addressed in Table 1, the components of the right hand side of equation (21) are computed for the explanatory parameters of the rainfall wavelet coefficients, at the scale of λ_c = 8 km. It can be observed that for the studied storm, knowing the range of variability of the orographic index, the variance of estimation error can be improved on the average by up to ~10% and 35% for α and s, respectively.

6. Conclusions

[40] The motivation for this research was to explore the linkages between the space-time statistical structure of precipitation and its underlying topography at multiple scales. This allows us to extract knowledge that can inform an efficient and accurate downscaling scheme of satellite precipitation products, such as those anticipated by the Global Precipitation Measuring (GPM) Mission, for hydrologic applications over complex terrain. In this study, we analyzed the Rapidan Storm of June 1995, over the

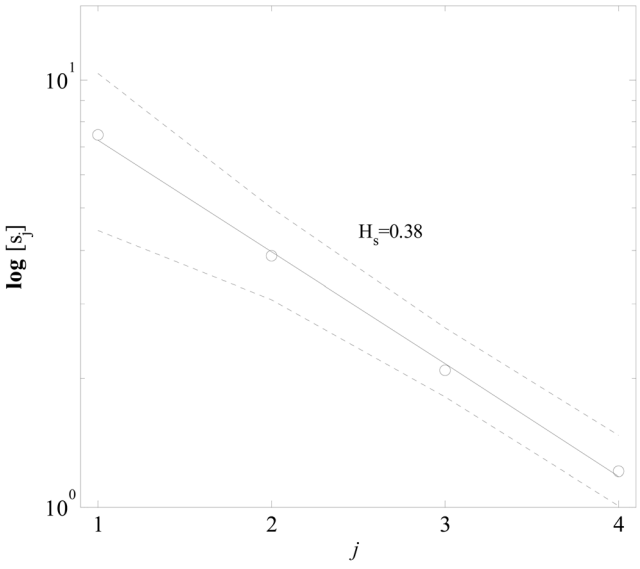

Figure 16. Scaling properties of the width parameter of the fitted generalized Gaussian (GG) distribution. Open circles show the mean values, and the dashed lines represent the corresponding 95% confidence intervals of the estimates. Given that the tail parameter α remains invariant at different scales and knowing the scaling law of the second-order moment (see Figure 14), the scaling of the width parameter s can be derived using $\mathrm{E}[X^2] = s^2\Gamma(3/\alpha)/\Gamma(1/\alpha)$. H_s denotes the scaling index of the width parameter.

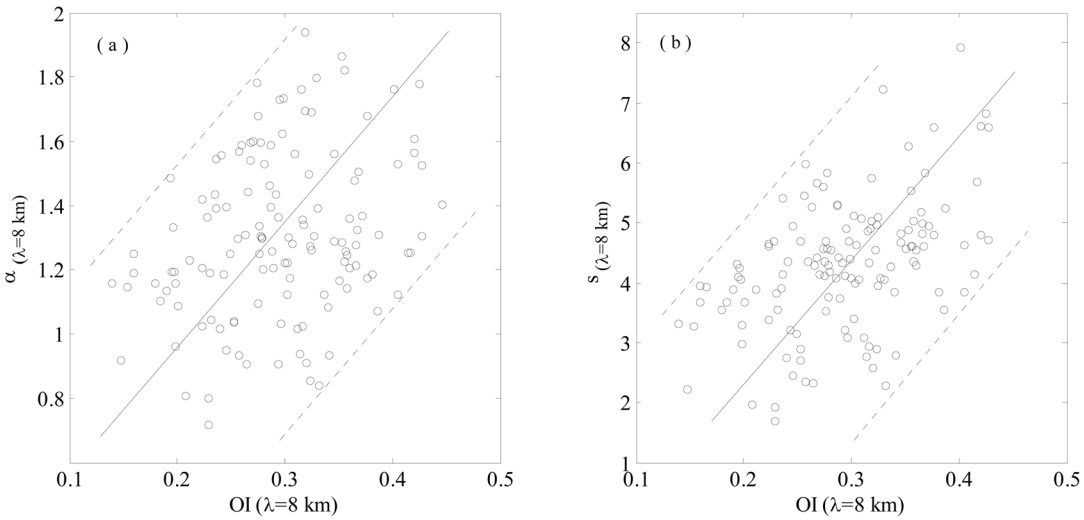

Figure 17. (a) The tail and (b) the width parameters of the fitted generalized Gaussian distribution to the wavelet coefficients of the log-transformed rainfall data at the scale λ_c = 8 km, plotted versus the orographic index computed at the same scale.

Appalachian Mountains, in terms of its multiscale statistical structure and its dependence on the underlying topography. First, to quantify the signature of the underlying elevation on the first- and second-order statistics of the rainfall field, a thresholding operation was performed to define cells of varying size and intensity. It was revealed that the spatial statistics of the rain cells' intensity values (i.e., mean and variance) had a strong dependence on the underlying elevations. Specifically, it was shown that the presence of orographic features accelerated locally the intensity and variability of rain cells and made their formation more likely above higher elevations. Subsequently, formal ways of analyzing the second-order scaling properties of the rainfall fields were presented both in Fourier and real space. The anisotropy of the two-dimensional Fourier spectrum and its directional dependence on the underlying terrain was explained. It was also shown how the variogram and directionally averaged spectrum of a scaling field relate to each other and can be estimated consistently in the context of remotely sensed rainfall images.

Table 1. Nonparametric Conditional Expectation of the Parameters $\theta \in \{\alpha, s\}$ of the GG Distribution With Respect to the Orographic Index[a]

	$E[\theta\|OI_k]$		$[E(\theta\|OI_k) - E(\theta)]^2/Var(\theta)$	
$OI(\lambda_c = 8$ km)	α	s	α	s
≤0.20	1.29	3.90	0.018	0.149
0.20–0.25	1.18	3.60	0.295	0.442
0.25–0.30	1.39	4.32	0.065	0.000
0.30–0.35	1.29	4.20	0.015	0.012
0.35–0.40	1.34	4.90	0.004	0.306
≥0.40	1.46	5.47	0.277	1.171
$E[E(\theta\|OI_k) - E(\theta)]^2/Var(\theta)$			0.11	0.35

[a]It is shown quantitatively that the variance of estimation can be a reduced appreciably by conditioning on the information content of the underlying topography.

[41] Coarse graining of the log-transformed rainfall fields revealed departure from Gaussianity, requiring special attention to the scaling of extremes. Haar wavelet decomposition of the log-transformed precipitation fields was performed and the generalized Gaussian (GG) distribution was found a suitable probability model which adequately explains the tails of the distribution of the wavelet coefficients over a range of scales.

[42] We also quantified the dependence of the parameters required for statistical downscaling of the precipitation fields on the underlying orographic features and showed that these parameters can be estimated more accurately by conditioning on the information content of the underlying topographic elevations. Obviously, since this study is just centered on a particular storm, our statistical descriptions are far from complete and provide the motivation for future generalization efforts through collecting and analyzing a large, statistically representative data set, and/or rainfall fields simulated via cloud-resolving models over orographic terrain.

[43] As a concluding remark, it is noted that in most of the available stochastic rainfall downscaling models using random cascade formalisms one of the main assumptions is the scale-to-scale independence of the random components (multipliers) of the cascade generator. Studies of natural images have shown that these random components may exhibit higher-order dependence, even though they are uncorrelated, and thus might require scale-dependent probabilistic characterizations [e.g., *Huang and Mumford*, 1999; *Wainwright and Simoncelli*, 2000]. Given the results of the presented study, it is worth exploring whether a scale-dependent cascade generator parameterized via the underlying terrain orographic information could be an avenue for improving rainfall downscaling schemes with emphasis on preservation of extremes.

[44] **Acknowledgments.** This work was supported by a NASA-GPM award NNX07AD33G and NSF award EAR-05366219 to the National Center for Earth-Surface Dynamics, an NSF Science and Technology

Center. In addition, computations of this research were partly supported by the University of Minnesota Supercomputing Institute for Advanced Computational Research. We also thank James Smith at Princeton University for providing us with the Rapidan storm radar data and Roberto Deidda for helpful comments. The senior author acknowledges the generous support of the Joseph T. and Rose S. Ling Chair in Environmental Engineering at the University of Minnesota.

References

Abry, P., and F. Sellan (1996), The wavelet-based synthesis for the fractional Brownian motion proposed by F. Sellan and Y. Meyer: Remarks and fast implementation, *Appl. Comput. Harmon. Anal.*, *3*(4), 377–383, doi:10.1006/acha.1996.0030.

Abry, P., S. Jaffard, and B. Lashermes (2004), Revisiting scaling, multifractal, and multiplicative cascades with the wavelet leader lens, *Proc. SPIE Int. Soc. Opt. Eng.*, *5607*, 103–117, doi:10.1117/12.581234.

Badas, M. G., R. Deidda, and E. Piga (2006), Modulation of homogeneous space-time rainfall cascades to account for orographic influences, *Nat. Hazards Earth Syst. Sci.*, *6*, 427–437, doi:10.5194/nhess-6-427-2006.

Barros, A. P., and R. J. Kuligowski (1998), Orographic effects during a severe wintertime rainstorm in the Appalachian Mountains, *Mon. Weather Rev.*, *126*, 2648–2672, doi:10.1175/1520-0493(1998)126<2648:OEDASW>2.0.CO;2.

Beran, J. (1994), *Statistics for Long-Memory Processes*, *Monogr. Stat. Appl. Prob.*, vol. 61, 315 pp., Chapman and Hall, New York.

Bousquet, O., and B. Smull (2003), Observations and impacts of upstream blocking during a widespread orographic precipitation event, *Q. J. R. Meteorol. Soc.*, *129*, 391–410, doi:10.1256/qj.02.49.

Deidda, R. (2000), Rainfall downscaling in a space-time multifractal framework, *Water Resour. Res.*, *36*(7), 1779–1784, doi:10.1029/2000WR900038.

Deidda, R., M. G. Badas, and E. Piga (2004), Space-time scaling in high-intensity Tropical Ocean Global Atmosphere Coupled Ocean-Atmosphere Response Experiment (TOGA-COARE) storms, *Water Resour. Res.*, *40*, W02506, doi:10.1029/2003WR002574.

Deidda, R., M. G. Badas, and E. Piga (2006), Space-time multifractality of remotely sensed rainfall fields, *J. Hydrol.*, *322*, 2–13, doi:10.1016/j.jhydrol.2005.02.036.

Flandrin, P. (1992), Wavelet analysis and synthesis of fractional Brownian motion, *IEEE Trans. Inf. Theory*, *38*(2), 910–917, doi:10.1109/18.119751.

Fristedt, B., N. Jain, and N. V. Krylov (2007), *Filtering and Prediction: A Primer*, *Student Math. Libr.*, vol. 38, 252 pp., Am. Math. Soc., Providence, R. I.

Gupta, V. K., and E. Waymire (1990), Multiscaling properties of spatial rainfall and river flow distributions, *J. Geophys. Res.*, *95*(D3), 1999–2009, doi:10.1029/JD095iD03p01999.

Gupta, V. K., and E. C. Waymire (1993), A statistical analysis of mesoscale rainfall as a random cascade, *J. Appl. Meteorol.*, *32*, 251–267, doi:10.1175/1520-0450(1993)032<0251:ASAOMR>2.0.CO;2.

Harris, D., M. Menabde, A. Seed, and G. Austin (1996), Multifractal characterization of rain fields with a strong orographic influence, *J. Geophys. Res.*, *101*(D21), 26,405–26,414, doi:10.1029/96JD01656.

Huang, J., and D. Mumford (1999), Statistics of natural images and models, paper presented at Conference on Computer Vision and Pattern Recognition, IEEE, New York.

Kaplan, L. M., and C.-J. Kuo (1993), Fractal estimation from noisy data via discrete fractional Gaussian noise (DFGN) and the Haar basis, *IEEE Trans. Signal Process.*, *41*, 3554–3562, doi:10.1109/78.258096.

Kumar, P., and E. Foufoula-Georgiou (1993a), A multicomponent decomposition of spatial rainfall fields: 1. Segregation of large- and small-scale features using wavelet transforms, *Water Resour. Res.*, *29*(8), 2515–2532, doi:10.1029/93WR00548.

Kumar, P., and E. Foufoula-Georgiou (1993b), A multicomponent decomposition of spatial rainfall fields: 2. Self-similarity in fluctuations, *Water Resour. Res.*, *29*(8), 2533–2544, doi:10.1029/93WR00549.

LeCam, L. (1961), A stochastic description of precipitation, paper presented at 4th Berkeley Symposium on Mathematical statistics and Probability, Univ. of Calif., Berkeley.

Lin, Y., S. Chiao, T. Wang, M. L. Kaplan, and R. P. Weglarz (2001), Some common ingredients for heavy orographic rainfall, *Weather Forecast.*, *16*, 633–660, doi:10.1175/1520-0434(2001)016<0633:SCIFHO>2.0.CO;2.

Lovejoy, S., and B. Mandelbrot (1985), Fractal properties of rain and a fractal model, *Tellus, Ser. A*, *37*, 209–232, doi:10.1111/j.1600-0870.1985.tb00423.x.

Lovejoy, S., and D. Schertzer (1985), Generalized scale invariance in the atmosphere and fractal models of rain, *Water Resour. Res.*, *21*(8), 1233–1250, doi:10.1029/WR021i008p01233.

Mallat, S. (1989), A theory for multiresolution signal decomposition: The wavelet representation, *IEEE Trans. Pattern Anal. Mach. Intell.*, *11*, 674–693, doi:10.1109/34.192463.

Mandelbrot, B. B., F. Adlai, and L. Calvet (1997), A multifractal model of asset return, *Cowles Found. Discuss. Pap. 1164*, 31 pp., New Haven, Ct.

Montgomery, D. R., G. Balco, and S. D. Willett (2001), Climate, tectonics, and the morphology of the Andes, *Geology*, *29*, 579–582, doi:10.1130/0091-7613(2001)029<0579:CTATMO>2.0.CO;2.

Nadarajah, S. (2005), A generalized normal distribution, *J. Appl. Stat.*, *32*(7), 685–694, doi:10.1080/02664760500079464.

Nykanen, D. K., and D. Harris (2003), Orographic influences on the multiscale statistical properties of precipitation, *J. Geophys. Res.*, *108*(D8), 8381, doi:10.1029/2001JD001518.

Over, T. M., and V. K. Gupta (1994), Statistical analysis of mesoscale rainfall: Dependence of a random cascade generator on large-scale forcing, *J. Appl. Meteorol.*, *33*, 1526–1542, doi:10.1175/1520-0450(1994)033<1526:SAOMRD>2.0.CO;2.

Perica, S., and E. Foufoula-Georgiou (1996a), Linkage of scaling and thermodynamic parameters of rainfall: Results from midlatitude mesoscale convective systems, *J. Geophys. Res.*, *101*(D3), 7431–7448, doi:10.1029/95JD02372.

Perica, S., and E. Foufoula-Georgiou (1996b), Model for multiscale disaggregation of spatial rainfall based on coupling meteorological and scaling descriptions, *J. Geophys. Res.*, *101*(D21), 26,347–26,361, doi:10.1029/96JD01870.

Pontrelli, M. D., G. Bryan, and J. M. Fritsch (1999), The Madison County, Virginia, flash flood of 27 June 1995, *Weather Forecast.*, *14*, 384–404, doi:10.1175/1520-0434(1999)014<0384:TMCVFF>2.0.CO;2.

Purdy, J. C., D. Harris, G. L. Austin, A. W. Seed, and W. Gray (2001), A case study of orographic rainfall processes incorporating multiscaling characterization techniques, *J. Geophys. Res.*, *106*(D8), 7837–7845, doi:10.1029/2000JD900622.

Rahman, M., and D. V. Gokhale (1996), On estimation of parameters of the exponential power family of distributions, *Commun. Stat. Simul. Comput.*, *25*(2), 291–299, doi:10.1080/03610919608813314.

Riedi, R. H., M. S. Crouse, V. J. Ribeiro, and R. G. Baraniuk (1999), A multifractal wavelet model with application to network traffic, *IEEE Trans. Inf. Theory*, *45*(3), 992–1018, doi:10.1109/18.761337.

Roe, G. H. (2005), Orographic Precipitation, *Annu. Rev. Earth Planet. Sci.*, *33*, 645–671, doi:10.1146/annurev.earth.33.092203.122541.

Ruderman, D. L. (1994), Statistics of natural images, *Network Comput. Neural Syst.*, *5*, 517–548, doi:10.1088/0954-898X/5/4/006.

Ruderman, D. L. (1997), Origins of scaling in natural images, *Vision Res.*, *37*(23), 3385–3398, doi:10.1016/S0042-6989(97)00008-4.

Smith, J. A., M. L. Baeck, M. Steiner, and A. J. Miller (1996), Catastrophic rainfall from an upslope thunderstorm in the central Appalachians: The Rapidan Storm of June 27, 1995, *Water Resour. Res.*, *32*(10), 3099–3113, doi:10.1029/96WR02107.

Subbotin, M. (1923), Subbotin: On the law of frequency errors, *Math. Sb.*, *31*, 296–301.

Veneziano, D., R. L. Bras, and J. D. Niemann (1996), Nonlinearity and self-similarity of rainfall in time and a stochastic model, *J. Geophys. Res.*, *101*(D21), 26,371–26,392, doi:10.1029/96JD01658.

Vianelli, S. (1963), La misura della variabilità condizionata in uno schema generale delle curve normali di frequenza, *Statistica*, *23*, 447–474.

Vianelli, S. (1983), The family of normal and lognormal distributions of order *r*, *Metron*, *41*, 3–10.

Wainwright, M. J., and E. P. Simoncelli (2000), Scale mixtures of Gaussians and the statistics of natural images, in *Advances in Neural Information Processing Systems*, vol. 12, edited by S. A. Solla, T. K. Leen, and K.-R. Muller, pp. 855–861, MIT Press, Cambridge, Mass.

Wieczorek, G. F., G. S. Mossa, and B. A. Morgan (2004), Regional debris-flow distribution and preliminary risk assessment from severe-storm events in the Appalachian Blue Ridge Province, USA, in Landslides, vol. 1, pp. 53–59, Springer, New York.

Wornell, G. W., and A. V. Oppenheim (1992), Estimation of fractal signals from noisy measurements using wavelets, *IEEE Trans. Signal Process.*, *40*, 611–623, doi:10.1109/78.120804.

Zhang, L., P. Bao, and X. Wu (2004), Wavelet estimation of fractional Brownian motion embedded in a noisy environment, *IEEE Trans. Inf. Theory*, *50*(9), 2194–2200, doi:10.1109/TIT.2004.833357.

M. Ebtehaj and E. Foufoula-Georgiou, Department of Civil Engineering, Saint Anthony Falls Laboratory, University of Minnesota–Twin Cities, 382 SAFL, Minneapolis, MN 55414-2196, USA. (efi@umn.edu)